

# Gravity wave temperature variance calculated using the ray-based spectral parameterization of convective gravity waves and its comparison with Microwave Limb Sounder observations

Hyun-Joo Choi,<sup>1</sup> Hye-Yeong Chun,<sup>1</sup> and In-Sun Song<sup>2,3</sup>

Received 20 October 2008; revised 23 December 2008; accepted 10 February 2009; published 24 April 2009.

[1] The ray-based spectral parameterization of convective gravity wave drag, which explicitly calculates the gravity wave propagation properties, is validated against the Microwave Limb Sounder (MLS) on the Upper Atmosphere Research Satellite (UARS). Offline calculations of the ray-based parameterization are performed using global reanalysis data and gravity wave temperature variances calculated from the parameterization are compared with those measured from the MLS. The parameterized temperature variances are calculated from gravity wave packets that are visible from the MLS to allow for comparison. The MLS visibility is analytically obtained using the three-dimensional MLS filter function. Comparisons between the parameterization calculations and MLS measurements show that both the magnitude and spatial distribution of the MLS-filtered temperature variances in the ray-based parameterization are in good agreement with observations. However, the MLS-filtered temperature variances are found to be sensitive to the source-level wave propagation direction, which, until now, has been regarded as a free parameter in the ray-based parameterization. This result indicates that the wave propagation direction can be crucial for more realistic parameterization of gravity wave (GW) effects and thus needs to be reasonably determined. Comparisons between the ray-based parameterization and columnar parameterization, which considers the gravity wave propagation only in the vertical direction, are also made in terms of temperature variance, and both results, after filtered, are similar to MLS observations. However, the magnitude of the unfiltered temperature variance in the equatorial regions with weak MLS visibility is smaller in the ray-based parameterization than in the columnar parameterization.

**Citation:** Choi, H.-J., H.-Y. Chun, and I.-S. Song (2009), Gravity wave temperature variance calculated using the ray-based spectral parameterization of convective gravity waves and its comparison with Microwave Limb Sounder observations, *J. Geophys. Res.*, **114**, D08111, doi:10.1029/2008JD011330.

## 1. Introduction

[2] Momentum transport by nonorographic gravity waves (GWs) is one of the crucial processes in the large-scale circulation of the middle atmosphere. However, nonorographic GWs are not fully resolved, even in modern general circulation models (GCMs). For this reason, the effects of unresolved nonorographic GWs have been parameterized in middle atmosphere GCMs [e.g., Hines, 1997; Kiehl *et al.*, 1996; Alexander and Dunkerton, 1999; Warner and McIntyre, 2001; Kim *et al.*, 2003].

[3] Among the various possible sources of nonorographic GWs, deep cumulus convection has been regarded as the

most prominent source with global distribution. The recognition of the importance of convectively forced GWs has led to the development of the parameterizations of gravity wave drag induced by cumulus convection (GWDC) [e.g., Chun and Baik, 1998, 2002; Beres, 2004; Song and Chun, 2005; Chun *et al.*, 2008]. Online tests of the GWDC parameterizations in some GCMs have shown that the GWDC parameterization can assist in more realistic simulations of the stratospheric and mesospheric climatology and variability [e.g., Chun *et al.*, 2001, 2004; Beres *et al.*, 2005; Song *et al.*, 2007].

[4] The current GWDC parameterizations, however, have limitations depending on column dynamics, which means that parameterized GWs are assumed to propagate only in the vertical direction at an (implicit) infinite vertical group velocity. To apply the column dynamics to GWD parameterization, as for most other physical parameterizations used in GCMs, can simplify the formulation and, in particular, make the efficient parallelization code. Hence, columnar GWDC parameterizations can only reflect partial characteristics of GWs. Horizontal and finite time propagation of GWs and

<sup>1</sup>Department of Atmospheric Sciences, Yonsei University, Seoul, South Korea.

<sup>2</sup>Goddard Earth Science and Technology Center, University of Maryland, Baltimore County, Baltimore, Maryland, USA.

<sup>3</sup>Global Modeling and Assimilation Office, NASA Goddard Space Flight Center, Greenbelt, Maryland, USA.

three-dimensional refraction is omitted in the columnar framework. To address this issue, *Song and Chun* [2008] (SC08 hereafter) developed a ray-based spectral parameterization of convective gravity wave drag. This parameterization is formulated on the basis of ray theory [e.g., *Lighthill*, 1978; *Marks and Eckermann*, 1995], so that it can consider GW propagation properties explicitly. SC08 implemented the ray-based parameterization into the NCAR Whole Atmosphere Community Climate Model version 1b [*Sassi et al.*, 2002] and showed that explicit consideration of GW propagation properties is important for more realistic simulations of stratospheric variability and zonal mean climatology.

[5] The ray-based parameterization is the most up-to-date and physically consistent approach which can most realistically represent the three-dimensional propagation of GWs among the GWDC parameterizations developed so far (SC08). However, there is still a great deal of uncertainty regarding the free parameters used in the ray-based parameterization. Therefore, the realism of the ray-based parameterization needs to be tested against observations. In the meantime, such validation will improve the ray-based parameterization by reducing uncertainties associated with its free-tuning parameters.

[6] For the validation of GW parameterization for global models, satellite observations have proven to be useful, as they can provide synoptic-scale observations of GW products [e.g., *Fetzer and Gille*, 1994; *Wu and Waters*, 1996; *Tsuda et al.*, 2000; *Ern et al.*, 2004; *Wu*, 2004; *Preusse et al.*, 2006; *Alexander and Teitelbaum*, 2007; *Alexander et al.*, 2008; *Wu and Eckermann*, 2008]. The synoptic-scale satellite measurements can be compared with the spatial distributions of particular GW sources such as convective clouds or orography [see *Jiang et al.*, 2004a, 2004b]. Such comparisons allow us to relate GW variances obtained from satellite observations to particular GW sources.

[7] Among the various instruments with the capability of measuring GW variances, the Microwave Limb Sounder (MLS) mounted on the Upper Atmosphere Research Satellite (UARS) has produced a significant number of measurements over convectively active geographical regions [e.g., *Wu and Waters*, 1996; *Alexander*, 1998; *McLandress et al.*, 2000; *Jiang et al.*, 2004b, 2005]. Some studies [e.g., *Alexander*, 1998; *McLandress et al.*, 2000] have shown that the MLS variances are well correlated with those of linear models that have nonorographic GW spectra, which includes convective sources. Also, MLS is appropriate for the purposes of the present study given that its measurement is sensitive to short horizontal wavelengths with which the GWDC parameterizations are mainly concerned.

[8] In this study, the ray-based parameterization is validated through the comparison of GW temperature variance (GWTV) between offline calculations of the parameterization using the reanalysis data and measurements from the MLS. As part of the validation procedure, we examine impacts of source-level wave propagation direction on GWTV with several sensitivity studies. The wave propagation direction is a prescribed parameter in the parameterization scheme. Finally, the GWTV calculated from the ray-based parameterization is also compared with that from the columnar

parameterization to evaluate the advantages of the ray-based parameterization.

## 2. Experimental Design

[9] Offline calculations of the ray-based parameterization are conducted for two periods (December–March (DJFM), 1992–1993 and June–September (JJAS), 1993). Observations of convective GWs for these two periods are taken from the UARS MLS observations reported by *Jiang et al.* [2004b].

[10] The overall procedure can be summarized as follows. First, GW properties and momentum flux spectra [*Song and Chun*, 2005] are specified at the source level (cloud top). Second, GW propagation is explicitly calculated using three-dimensional ray-tracing equations [*Lighthill*, 1978]. Finally, the time variation of the wave amplitude and the deposition of GW momentum fluxes into the ambient flow are computed using Lindzen-type saturation method [*Kiehl et al.*, 1996]. For further details, refer to SC08.

[11] The specification of GW spectra requires deep convective heating (DCH) and background flow. For the offline calculation, heating and background flow are taken from assimilation data sets. Convective heating is obtained from the 6-hourly DCH of the National Centers for Environmental Prediction (NCEP) Department of Energy (DOE) reanalysis 2 on T62 ( $192 \times 94$ ) quadratic Gaussian grids and 28 sigma levels (about 1000–2.5 hPa) [*Kanamitsu et al.*, 2002]. For the background atmosphere, we use the 6-hourly wind and temperature of the European Center for Medium-Range Weather Forecasts (ECMWF) ERA-40 reanalysis on  $2.5^\circ$  grids and 23 pressure levels (1000–1 hPa) [*Uppala et al.*, 2005]. The ECMWF wind and temperature are horizontally interpolated onto T62 Gaussian grids so that the wind and stability profiles required for calculating the momentum flux spectra can be defined at the same horizontal location where DCH exists. Although the ECMWF fields are linearly interpolated onto the T62 Gaussian grids without spectral filtering, it is found that the risk of aliasing is negligible (not shown).

[12] Convective GW packets are launched every 6 h at the top of deep convection. The height of the convection top is estimated from the vertical profile of the DCH (see *Song et al.* [2007] for details). The momentum flux at the cloud top is analytically formulated in a three-dimensional framework for the given diabatic forcing (with Gaussian shape) and basic-state wind and stability (three-layer atmosphere with low-level wind shear and constant buoyancy frequency in a forcing region and above) as a function of phase speeds and wave propagation direction ( $\phi$ ) (see *Song and Chun* [2005] for details). The cloud top momentum flux spectrum is determined by the spectral combination of diabatic forcing and wave-filtering-and-resonant factor (WFRF) that is determined by the basic-state wind and stability and vertical configuration of forcing. WFRF includes two physical meanings. First, it acts as a wave-filtering factor that controls the effectiveness of the diabatic source [*Song et al.*, 2003]. Second, WFRF represents resonance between the vertical harmonics consisting of forcing and natural wave modes with the vertical wave numbers given by the dispersion relation of internal gravity waves. Thus, the spectral shape of the cloud top momentum flux spectrum is deter-

mined by a combination of the WFRF and diabatic forcing according to the degree of overlapping between the two. The wave propagation direction  $\phi$  is defined as the angle measured counterclockwise from the east. In the ray-based parameterization, the wave propagation direction  $\phi$  at the cloud top is a free parameter, yet it will be shown that  $\phi$  can be constrained by comparison with MLS observations. Details are discussed in section 3.2.

[13] Stratospheric GWTVs ( $z = 38$  km) calculated from the offline ray-based parameterization are compared with the north looking ascending (NA) and south looking descending (SD) MLS limb-scan mode measurements at channels 3 and 13, as described by *Jiang et al.* [2004b]. The MLS channels 3 and 13 are a pair of wing channels of 63 GHz O<sub>2</sub> emission lines with saturation altitude of  $\sim 38$  km. To compare with the MLS GW variances, GWTVs from the ray-based parameterization are calculated by filtering out GW components not visible to the MLS. In this study, the MLS visibility is assumed to be given by the analytical filter function used by *Jiang et al.* [2004a]. This filter function was obtained for MLS limb-tracking mode in which the vertical tilt of the instrument line of sight (LOS) is fixed. On the other hand, the vertical tilt angle of the LOS varies with each measurement in the scanning mode, in which the MLS GWTVs used in this study are observed. Nonetheless, we use the filter function for the limb-tracking mode, and thus can avoid a complicated analytic treatment of the time-varying LOS angle. Also, the use of the limb-track filter instead of a limb-scan filter can be acceptable in practice considering the close similarities between the GWTVs from the scan and track modes for the along-track cutoff horizontal wavelength of 480 km [see *McLandress et al.*, 2000, Figure 1].

[14] Following *Jiang et al.* [2004a], the visibility for the MLS limb-track measurement ( $R$ ) is written as the following spectral filter function:

$$\begin{aligned} R(k_X, k_{Y'}, k_{Z'}) &= R_X(k_X) f^{1/2}(k_X^{-1}) R_{Y'}(k_{Y'}) R_{Z'}(k_{Z'}) \\ &= \exp \left[ -(\pi w_X k_X)^2 - (\pi w_{Y'} k_{Y'})^2 - (\pi w_{Z'} k_{Z'})^2 \right] \\ &\quad \cdot f^{1/2}(k_X^{-1}), \end{aligned} \quad (1)$$

where  $k_X (= \lambda_X^{-1})$  is the along-track wave number and  $k_{Y'}$  and  $k_{Z'}$  are the across-track and vertical wave numbers rotated by an effective LOS angle ( $\phi \sim -2.94^\circ$  for channels 3 and 13) around the along-track axis  $x$ .

[15] The three wave numbers ( $k_X$ ,  $k_{Y'}$ , and  $k_{Z'}$ ) in (1) are wave number components along axes defined by the MLS viewing geometry and satellite motion [see *Jiang et al.*, 2004a]. They are represented in a coordinate system defined by the effective MLS LOS ( $\phi$ ) and the UARS track angle ( $\alpha_T$ ). To apply (1) to each GW packet calculated in the usual coordinate system ( $x, y, z$ ) from the parameterization, the GW wave numbers ( $k, l, m$ ) for each GW packet from the parameterization are transformed into these wave numbers ( $k_X$ ,  $k_{Y'}$ , and  $k_{Z'}$ ) through two sequential rotational transformations as follows:

$$\begin{pmatrix} k_X \\ k_{Y'} \\ k_{Z'} \end{pmatrix} = \begin{pmatrix} 1 & 0 & 0 \\ 0 & \cos \phi & \sin \phi \\ 0 & -\sin \phi & \cos \phi \end{pmatrix} \begin{pmatrix} \cos \alpha_T & \sin \alpha_T & 0 \\ -\sin \alpha_T & \cos \alpha_T & 0 \\ 0 & 0 & 1 \end{pmatrix} \begin{pmatrix} k \\ l \\ m \end{pmatrix}, \quad (2)$$

where the track angle ( $\alpha_T$ ) is the angle measured counterclockwise from the east to the axis  $x$  along the UARS track. This formulation is identical to that used by *Jiang et al.* [2004a] except that  $\alpha_T$  is measured in the reverse direction for direct comparison between  $\alpha_T$  and the MLS visibility with respect to the wave propagation direction measured counterclockwise from the east (see Figure 3).

[16] In the formulation for  $R$  given in (1), the along-track axis  $x$  is defined to be along the UARS track, and the across-track axis  $y$  points toward the direction in which the MLS views. Since the MLS views at right angles to the UARS track, the  $y$  axis is perpendicular to the  $x$  axis. The actual direction of the  $x$  axis is determined so that the two axes ( $x$  and  $y$ ) together with the vertical  $z$  axis form a right-hand coordinate system (see *Jiang et al.* [2004a] for details). For example, if the MLS views in the northeastern (southwestern) direction following descending orbits, the  $x$  axis points toward the same (opposite) direction of the UARS track. The final MLS coordinate system ( $x, y', z'$ ) is obtained by rotating the coordinate ( $x, y, z$ ) around the  $x$  axis by the effective LOS angle  $\phi$ .

[17] In (1),  $f(\lambda_X)$  is an analytical function that accounts for MLS response for the six-point limb-track mode to along-track wavelengths ( $\lambda_X$ ), especially long wavelengths. This function is given by

$$f(\lambda_X) = \begin{cases} \frac{1 + (\lambda_2/\lambda_1)^p}{1 + (\lambda_X/\lambda_1)^p} & \text{for } \lambda_X \geq \lambda_2, \\ 1 & \text{for } \lambda_X < \lambda_2 \end{cases}, \quad (3)$$

where  $\lambda_1 = 100$  km,  $\lambda_2 = 60$  km, and  $p = 4.3$ . Although the MLS limb-scan data, which is used in this study, has a longer along-track wavelength cutoff than the six-point limb-track, it is found (with 480 km limb-tracking mode) that the GWTVs filtered by applying MLS visibility function in the parameterization are not largely sensitive to the wavelength cutoff (not shown).

[18] In addition,  $w_X$  in (1) is set to 12 km for comparison with MLS channels 3 and 13, and  $w_{Y'}$  and  $w_{Z'}$  in (1) are expressed as

$$w_{Y'} = w_C / [\sin^2 \phi + \gamma(\sin \phi - \beta \cos \phi)], \quad (4)$$

$$w_{Z'} = w_C / [\cos^2 \phi + \gamma(\cos \phi + \beta \sin \phi)], \quad (5)$$

where  $w_C$  ( $\approx 6.8$  km) is the half width at half maximum (HWHM) of Gaussian fit to the vertical temperature weighting function,  $\gamma = (w_C/w_b)^2$  (where  $w_b$  ( $\approx 4.85$  km) denotes the width of the MLS antenna), and  $\beta$  ( $= -4.53^\circ$ ) is the actual MLS LOS angle for channels 3 and 13.

[19] For the values of the parameters ( $\lambda_1$ ,  $\lambda_2$ ,  $p$ ,  $w_X$ ,  $w_{Y'}$ , and  $w_{Z'}$ ) given in (3)–(5), the detailed shape of the three-dimensional MLS visibility  $R$  can be depicted. In the direction of the  $\lambda_X$  axis, the structure of the  $R$  is given by  $R_X f^{1/2}$ .  $R_X f^{1/2}$  has a peak at  $\lambda_X \approx 70$  km, which means that the MLS visibility has the largest value at  $\lambda_X \approx 70$  km in the direction of  $\lambda_X$ . The function  $R_X f^{1/2}$  increases rapidly (decreases slowly) with  $\lambda_X$  for  $\lambda_X < 70$  km ( $> 70$  km). On the  $\lambda_{Y'} - \lambda_{Z'}$  surface, the structure of  $R$  is determined by the two dimensional function  $R_{Y'} R_{Z'}$ . The illustration for the



function  $R_Y R_Z$  (not shown) shows that the MLS has large sensitivity at  $\lambda_Y$  values larger than about 150 km and at  $\lambda_Z$  values larger than 10 km. Further details on the structure of the  $R$  is given by Jiang *et al.* [2004a].

[20] The MLS-filtered GWTV at a spatial position is defined as the sum of the MLS-filtered temperature variances ( $T_f'^2$ ) due to rays located at each grid point. The  $T_f'^2$  due to each ray is obtained by applying the MLS spectral visibility  $R$  to the temperature perturbations ( $T'$ ) associated with the ray. The amplitude of  $T'$  for each ray is reduced by applying the MLS visibility  $R$ . As a result, the MLS-filtered GWTV is given as follows:

$$GWTV = \sum \overline{T_f'^2} = \sum \overline{[RT'(k, l, m)]^2}, \quad (6)$$

where the sum is over the individual rays at the observational location.

### 3. Results

#### 3.1. Comparison With MLS Measurements

[21] Figure 1 shows the time-averaged GWTV at  $z = 38$  km, obtained from the MLS limb-scan NA and SD measurements over subtropical clouds [Jiang *et al.*, 2004b], the maximum NCEP DCH in the troposphere, and unfiltered and filtered GWTVs calculated using the ray-based parameterization for DJFM, 1992–1993 and JJAS, 1993, respectively.

[22] The NCEP DCH is used as an indicator for deep convection. The use of the NCEP DCH might degrade the reliability of the results of the present study because any observations regarding the DCH are not involved in the production of the NCEP reanalysis. In fact, the DCH depends significantly on the physics schemes of a global model used to produce NCEP reanalysis. However, realism issues related to the NCEP DCH are unlikely to be serious, as the DCH correlates well with observed spatial distributions from the NOAA Climate Prediction Center Merged Analysis of Precipitation (CMAP) (see CMAP in Figure 1).

[23] The MLS GWTV exhibits peaks over broad regions only in the summer subtropics, and is almost zero in the equatorial regions despite strong tropical convection (see the NCEP DCH). Many MLS studies [e.g., Alexander, 1998; McLandress *et al.*, 2000; Jiang *et al.*, 2005] have also reported the subtropical variance enhancements (weak tropical variances) shown in the MLS NA and SD measurements, with these results being attributed to strong (weak) background winds in the subtropical (equatorial) regions. Since strong background winds can lead to waves refracted to long vertical wavelengths, which are more visible to MLS (via refraction), it is reasonable to relate wind strength to MLS GW visibility. Similar features were also noted in the GWTV measured from new MLS instrument on the Aura satellite by Wu and Eckermann [2008], despite instrumental and viewing differences. They showed that the tropical variances over tropical deep convection are enhanced mainly in the lower stratosphere and that the upper stratospheric variances from convective GWs are enhanced toward the summer subtropics because of the filtering and refraction of GWs by strong subtropical stratospheric winds.

[24] The unfiltered GWTVs (see ray-based GWTV (unfiltered) in Figure 1) represent the GWTVs from the ray-based

parameterization before the MLS filter is applied. For this calculation, an appropriate value ( $= 375$ ) is specified for the conversion factor (i.e.,  $c_f$  in the work of Song *et al.* [2007]) to determine the overall magnitude of convective GWs from the magnitude of the DCH. The source-level wave horizontal propagation azimuth angles ( $\phi$  values) are set to  $45^\circ$  and  $135^\circ$  to best reproduce the MLS GWTVs in the ray-based parameterization (see section 3.2 for MLS reproducibility of the ray-based parameterization with respect to the wave propagation direction). The unfiltered GWTVs are about 50 times (or more) larger than the observed, peaking above strong convection in the equatorial regions. However, the magnitude of the GWTVs is significantly reduced by applying the MLS filter function, especially in the equatorial regions with weak MLS visibility similar to the response noted for orographic GWTVs by Jiang *et al.* [2004a] (see section 3.2 for the MLS visibility). The MLS-filtered GWTVs (see ray-based GWTV (filtered) in Figure 1) exhibit similar spatial distributions and magnitudes to the MLS GWTVs, except for a slight overestimation in the MLS-filtered GWTVs over the northern subtropical regions for DJFM, 1992–1993, and over the equatorial regions for JJAS, 1993. The unrealistic features can be attributed to the overestimated NCEP DCH in these regions, compared with CMAP precipitation, and uncertainties regarding unknown parameters in the parameterization. This indicates that the ray-based parameterization can reproduce the observed MLS GWTVs reasonably well with appropriately specified parameters (i.e.,  $c_f = 375$  and  $\phi = 45^\circ$  and  $135^\circ$ ).

#### 3.2. Sensitivity to Wave Propagation Direction

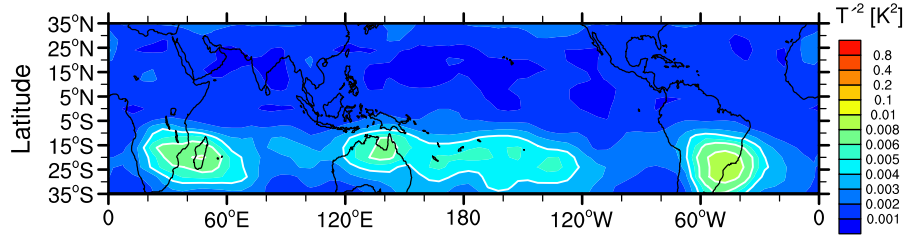
[25] Although the ray-based parameterization has the capability of reproducing the observed MLS GWTVs, the reproducibility depends on the source-level wave propagation direction, which is a free parameter in the ray-based parameterization. In this section, we investigate the sensitivity of the MLS-filtered GWTV calculated from the ray-based parameterization to the wave propagation direction ( $\phi$  values).

[26] Figure 2 shows the MLS GWTV and MLS-filtered GWTV from the ray-based parameterization with four different wave propagation directions ( $\phi = (1) 45^\circ$ , (2)  $45^\circ$  and  $135^\circ$ , (3)  $135^\circ$ , and (4)  $0^\circ$  and  $90^\circ$ ) at  $z = 38$  km, averaged over DJFM, 1992–1993 and JJAS, 1993, respectively. The reproduction is best when two  $\phi$ s of  $45^\circ$  and  $135^\circ$  are used, as in Figure 1. Comparison of the results from the four sensitivity tests shows that the MLS GWTVs are due mainly to GWs with  $\phi = 135^\circ$  for DJFM and  $45^\circ$  for JJAS in the ray-based parameterization. On the other hand, with  $\phi = 0^\circ$  and  $90^\circ$ , which are used in SC08, the MLS-filtered GWTV is overestimated in the equatorial regions and underestimated in the summer subtropics.

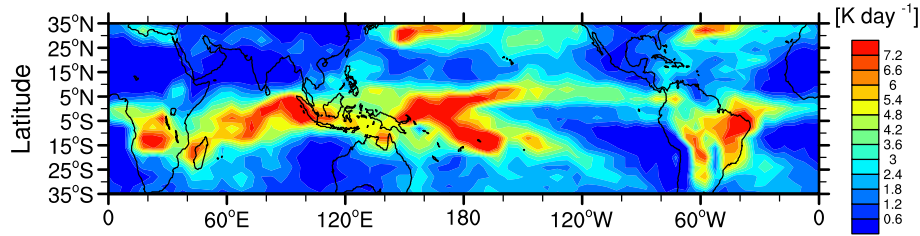
[27] The MLS-filtered GWTV is determined as a combination of the MLS visibility and GWTV calculated from the ray-based parameterization, and both are sensitive to the wave propagation direction. The dependence of the MLS visibility on GW propagation direction has been reported in many studies [e.g., McLandress *et al.*, 2000; Jiang *et al.*, 2004a; Wu and Eckermann, 2008]. They demonstrated that the magnitude and spatial structure of GWTVs observed by MLS are significantly influenced by the horizontal propagation direction of the GWs.

**(a) DJFM, 1992–1993**

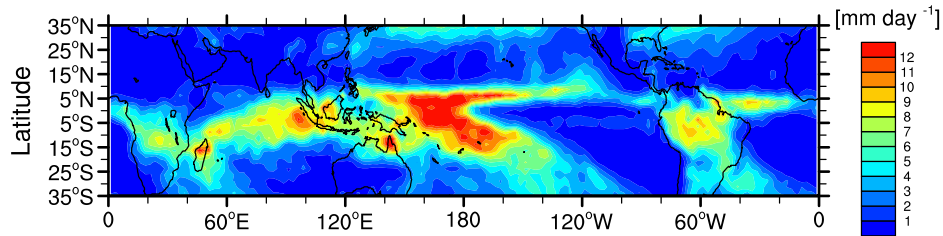
MLS GWTV



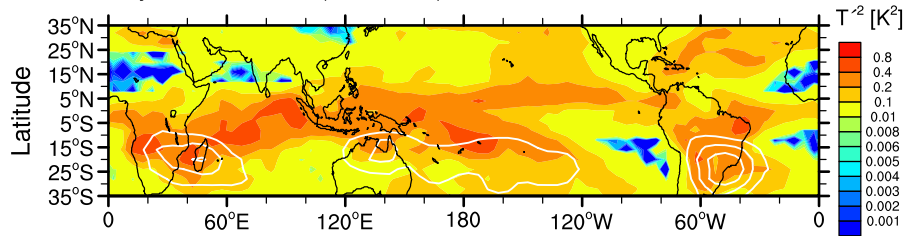
NCEP DCH



CMAP



Ray-based GWTV (Unfiltered)



Ray-based GWTV (Filtered)

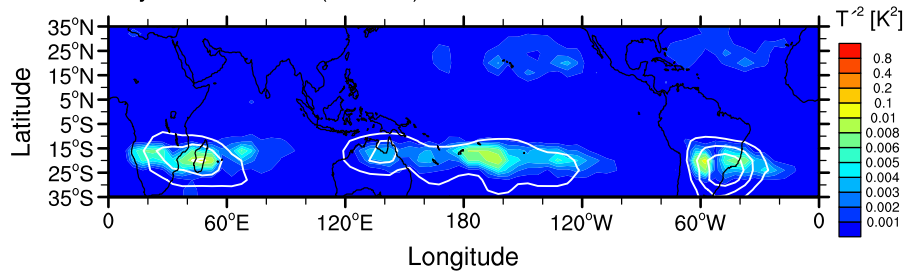


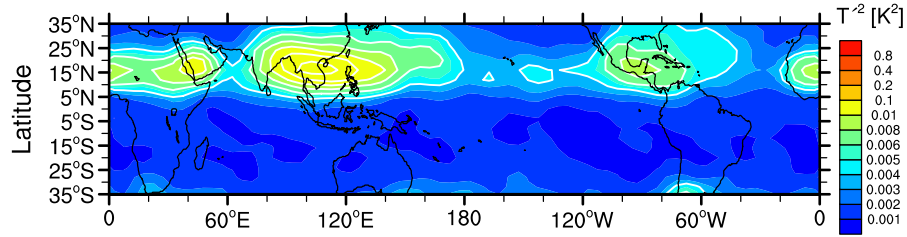
**Figure 1.** Time-averaged MLS GWTV at a pressure height of  $z = 38$  km taken from *Jiang et al.* [2004b], the maximum NCEP DCH, mean precipitation from the NOAA Climate Prediction Center Merged Analysis of Precipitation (CMAP), and unfiltered and MLS-filtered GWTVs at  $z = 38$  km in the ray-based parameterization for (a) December–March, 1992–1993 and (b) June–September, 1993. The thick white lines denote the contours of the MLS GWTV with 0.004, 0.006, 0.008, 0.01, 0.012, and 0.014  $\text{K}^2$ .

[28] To comprehend the dependence of the MLS-filtered GWTV on wave propagation direction, we separately investigate the sensitivity of the MLS visibility and GWTV from the parameterization to the wave propagation direction. First, we examine the sensitivity of the MLS visibility to the horizontal wave propagation direction. The spectral

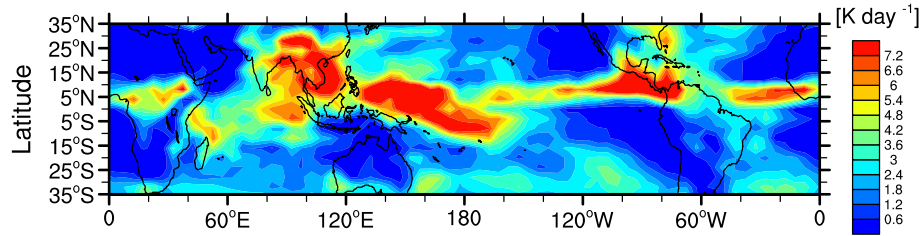
MLS visibility given in (1) is a complicated function of wavelengths. Hence, to simplify the discussion, we consider a specific monochromatic GW packet with a horizontal wavelength ( $\lambda_h$ ) of 80 km and a vertical wavelength ( $\lambda_z$ ) of 20 km (these wavelengths are in the range of wavelengths that is observed well by the MLS limb-track measurement,

## (b) JJAS, 1993

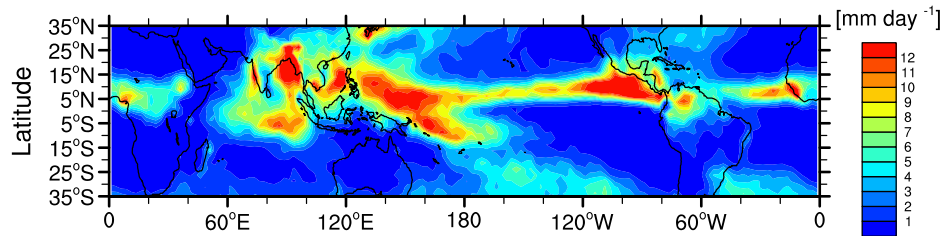
MLS GWTV



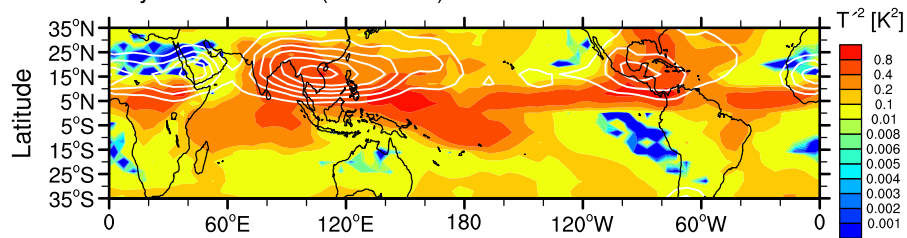
NCEP DCH



CMAP



Ray-based GWTV (Unfiltered)



Ray-based GWTV (Filtered)

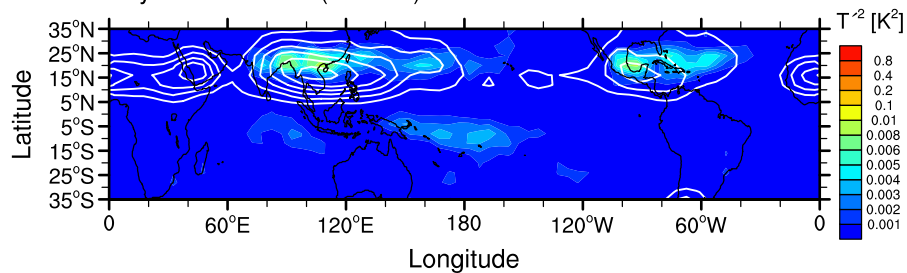


Figure 1. (continued)

for which the visibility function is applied in this study). For a given value of  $\varphi$ ,  $(k, l)$  is determined as  $2\pi/[\lambda_y(\cos \varphi, \sin \varphi)]$ , and  $m$  is set to  $-2\pi/\lambda_z$  (we assume upward propagating waves, i.e.,  $m < 0$ ). As a result, the vector  $(k, l, m)$  can be regarded as a function of  $\varphi$ . Since  $R$  is a function of the vector  $(k, l, m)$  as shown in (1)–(2),  $R$  must also be a function of  $\varphi$ . In addition, the calculation of  $R$  requires the specification of  $\alpha_T$ , which is provided by D. L. Wu (personal communications, 2008), and can be, to a good approximation, regarded as a function of latitude alone, as shown by Jiang *et al.* [2004a,

Figure 7]. Therefore, the MLS visibility  $R$  can be viewed as a function of wave propagation direction and latitude.

[29] Figure 3a shows the MLS visibility for the monochromatic GW packet plotted on a two-dimensional grid of NCEP Gaussian latitude and wave propagation direction for the NA and SD orbits, respectively, following a very similar presentation given by Jiang *et al.* [2004a, Figure 10]. The MLS visibility with respect to wave propagation direction shows that the MLS visibility is especially strong when GWs propagate along the track angle, though there is a large



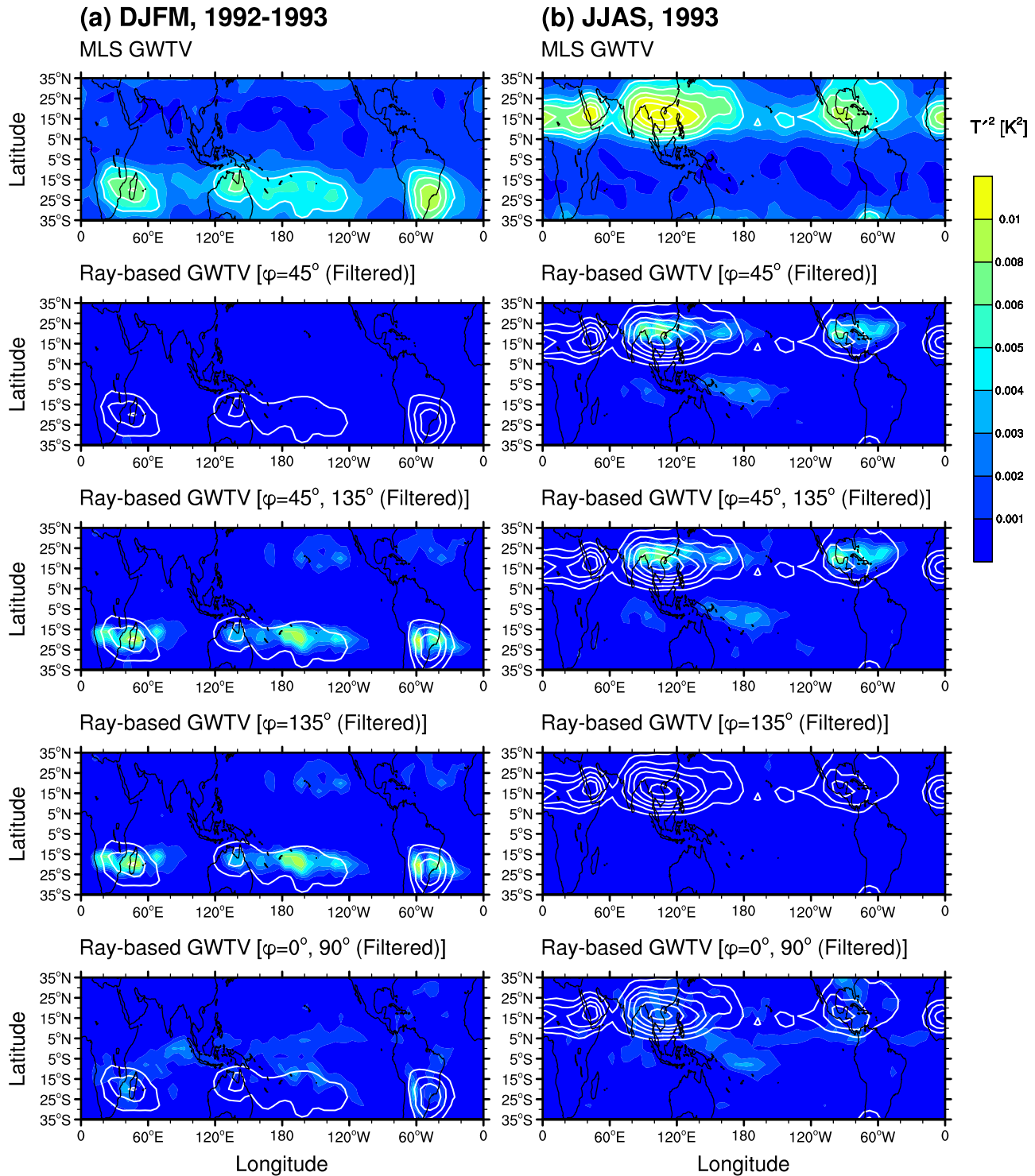


**Figure 2.** Time-averaged MLS and MLS-filtered ray-based GWTVs at  $z = 38$  km for (a) December–March 1992–1993 and (b) June–September 1993. Wave propagation directions ( $\phi$  values) of  $45^\circ$ ,  $45^\circ$  and  $135^\circ$ ,  $135^\circ$ , and  $0^\circ$  and  $90^\circ$  are considered, respectively. The thick white lines denote the contours of the MLS GWTV with 0.004, 0.006, 0.008, 0.01, 0.012, and 0.014  $\text{K}^2$ .

asymmetry to the visibility, such that the visibilities at  $\pm 10^\circ$  away from the track angle are different from each other. This shows that the MLS measurement detects GWs propagating along the satellite track much more accurately than GWs propagating in any other direction.

[30] Next, we examine the sensitivity of the parameterized GWTV to the wave propagation direction for 15 December 1992 and 15 August 1993, 2 days on which MLS NA and SD measurements are made, respectively. For each day, we perform the offline calculations of the

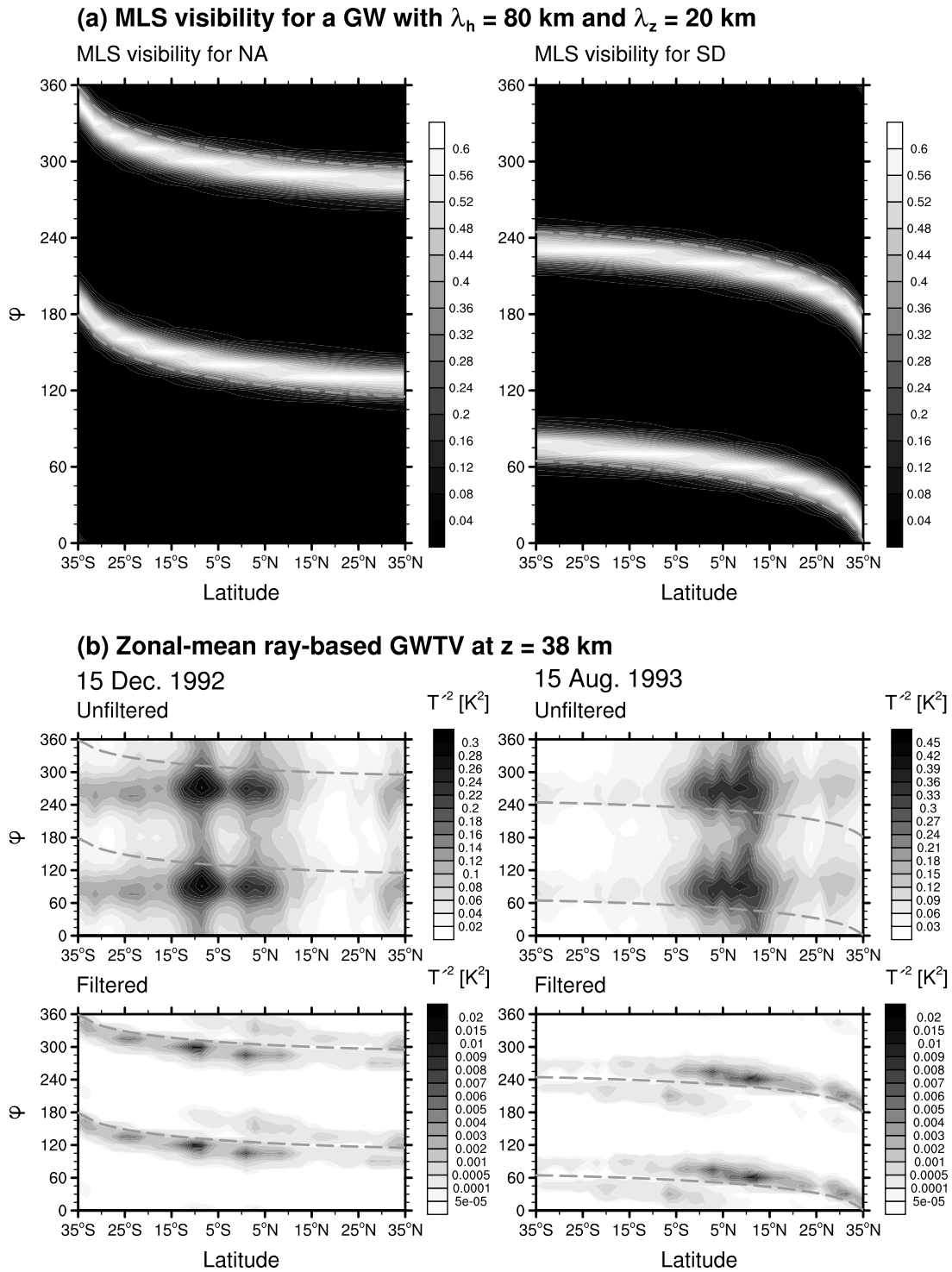


**Figure 3.** (a) MLS visibility for a monochromatic GW packet (with a horizontal wavelength of 80 km and a vertical wavelength of 20 km) as a function of latitude and wave propagation direction for north looking ascending and south looking descending orbits, respectively. (b) Zonal mean unfiltered and MLS-filtered GWTVs at  $z = 38$  km in the ray-based parameterization for 15 December 1992 and 15 August 1993, respectively. The grid interval for wave propagation direction is set to  $10^\circ$  and  $15^\circ$  in Figures 3a and 3b, respectively. Angles ( $\alpha_T$  and  $\alpha_T - 180^\circ$ ) for the two possible propagation directions along the track angle ( $\alpha_T$ ) are overplotted with gray dashed lines in Figures 3a and 3b.



ray-based parameterization for individual wave propagation directions binned at  $15^\circ$  intervals. Figure 3b shows zonal mean unfiltered and MLS-filtered GWTVs at  $z = 38$  km, calculated from the ray-based parameterization as a function of latitude and wave propagation direction for the 2 days. Strong unfiltered GWTVs appear in the equatorial regions and summer subtropics because of strong convective sources. The unfiltered GWTVs are found to be much stronger at  $\varphi = 90^\circ$  and  $270^\circ$  than in any other direction. This is likely to be due to weak critical-level filtering associated with weak meridional wind.

[31] Although the unfiltered GWTVs are strong at  $\varphi = 90^\circ$  and  $270^\circ$ , the peaks of the MLS-filtered GWTVs are concentrated near two wave propagation directions ( $\alpha_T$  and  $\alpha_T - 180^\circ$ ) related to the track angle. This can be understood from the combination of the MLS visibility in Figure 3a and the unfiltered GWTVs. Although the MLS visibility in Figure 3a is for a specific monochromatic GW packet, it can approximately represent the overall pattern for whole spectral ranges since the MLS visibility is significantly strong near  $\lambda_h = 80$  km and  $\lambda_z = 20$  km. The combination of the MLS visibility and the unfiltered GWTVs produces strong MLS-filtered GWTVs at wave propagation directions within about  $30^\circ$  either side of  $\alpha_T$  or  $\alpha_T - 180^\circ$  in the equatorial regions and the summer subtropics. The peak of the MLS-filtered GWTV in the summer subtropics appears near a wave propagation direction of  $135^\circ$  ( $45^\circ$ ) for 15 December 1992 (15 August 1993). This is consistent with the results shown in Figure 2, where the strong MLS GWTV in the summer subtropics is best reproduced in the ray-based parameterization with  $\varphi = 45^\circ$  and  $135^\circ$  for DJFM, 1992–1993 and JJAS, 1993. This result also indicates that it is important to determine the wave propagation direction reasonably well in order to realistically reproduce GW effects using the ray-based parameterization.

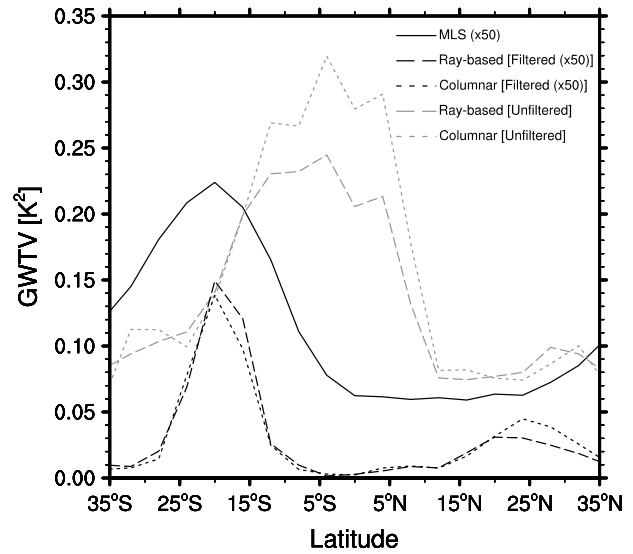
### 3.3. Comparison With Columnar Parameterization

[32] In this section, the GWTV parameterized through the ray-based parameterization is compared with the columnar parameterization, which is based on the work of *Song and Chun* [2005]. For this, we perform an additional offline calculation of the columnar spectral parameterization. The columnar and ray-based parameterizations share identical momentum flux spectra and physical processes regarding the elimination of GWs (e.g., saturation, wave reflection and WKB violation, see SC08 for details).

[33] Figure 4a shows zonal mean MLS GWTVs and unfiltered and filtered GWTVs at  $z = 38$  km, calculated from the ray-based and columnar parameterizations. The unfiltered GWTVs in both parameterizations are about 50 times (or more) larger than the MLS GWTVs peaking in the equatorial regions. Although the distributions of the unfiltered GWTVs in both parameterizations are similar, the magnitude in the equatorial regions is smaller in the ray-based parameterization. This difference is mainly due to the smaller number of GW packets in the ray-based parameterization (see Figure 4b), which can be attributed to the suppression of vertical propagation by the concentration of the ray packets into the lower stratosphere and troposphere due to explicitly calculated GW propagation and enhanced filtering of GW packets in the ray-based parameterization. This result is consistent with that in SC08, where it was shown that

## DJFM, 1992–1993

(a) Zonal-mean GWTV at  $z = 38$  km



(b) Number of ray packets at  $z = 38$  km

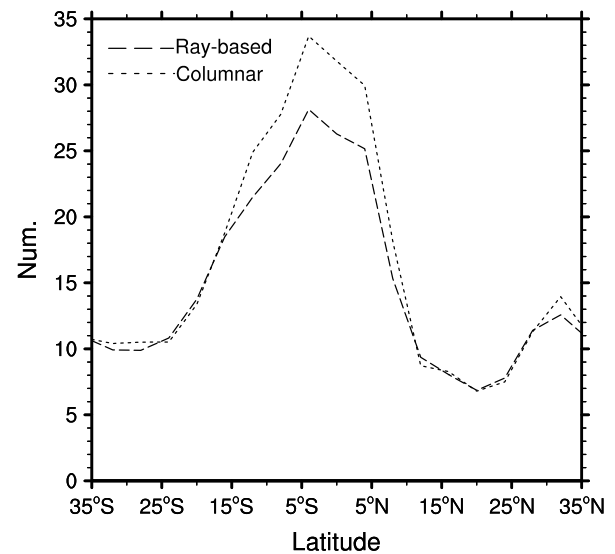


**Figure 4.** (a) Zonal mean MLS (black solid), unfiltered ray-based (gray dashed), unfiltered columnar (gray dotted), MLS-filtered ray-based (black dashed), and MLS-filtered columnar (black dotted) GWTVs at  $z = 38$  km and (b) zonal mean number of ray packets at  $z = 38$  km in the ray-based (dashed) and columnar (dotted) parameterizations, averaged over December–March, 1992–1993. The MLS GWTV and MLS-filtered GWTVs in the ray-based and columnar parameterizations are multiplied by a factor of 50.

stronger wave drag can be produced in the equatorial lower stratosphere in the climate model with the ray-based parameterization, because of the enhanced filtering of GWs concentrated into the lower stratosphere. The GWTV difference in the equatorial regions between the two parameterizations increases and extends to the subtropical regions with height (not shown). This difference implies that the limitations of the columnar parameterization may lead to excessive forcing in the middle atmosphere directly above source regions in the

troposphere. In addition, this also implies that the horizontal propagation of convective GWs is significant at the equatorial and subtropical regions.

[34] In both parameterizations, however, the magnitude and distribution of the MLS-filtered GWTVs are similar, despite the differences between the unfiltered GWTVs in the equatorial regions. This is because the unfiltered GWTVs in the equatorial regions hardly contribute to the MLS-filtered GWTVs, because of the weak MLS visibility for equatorial GWs. Instead, in both parameterizations, similar MLS-filtered GWTVs are produced by similar magnitudes of unfiltered GWTVs in the summer subtropics, where the higher MLS visibility for convective GWs appears. Also, the MLS-filtered GWTVs in both parameterizations agree relatively well with the observed MLS GWTV, compared with the unfiltered GWTVs. Although both the ray-based and columnar parameterizations can reasonably reproduce the MLS GWTVs, it should be noted that comparison with the MLS is limited to the subtropics at only one height ( $z = 38$  km) in the upper stratosphere. In particular, GWTVs from the two parameterizations are required for a comparison with MLS GWTVs at heights lower than  $z = 38$  km, since equatorial variances for convective GWs are enhanced in the lower stratosphere [see *Wu and Eckermann, 2008*]. However, the UARS MLS unfortunately cannot observe this equatorial enhancement in the lower-stratospheric GW variance because of instrumental limitations as discussed by *Wu and Eckermann [2008]*. Consequently, the realism of each parameterization and the differences between the two parameterizations cannot be fully assessed through comparison with the UARS MLS data alone. Additional comparisons with GW observations from other instruments are required to clearly understand the differences between the two parameterizations.

#### 4. Summary and Discussion

[35] In this study, we compared the ray-based GW parameterization to the UARS MLS measurements of stratospheric GW activity. We carried out an offline calculation of the ray-based parameterization using the ray-based parameterization and global NCEP/NCAR and ECMWF reanalysis data sets for DJFM, 1992–1993 and JJAS, 1993, respectively. The GWTVs calculated from the parameterization were filtered by the three-dimensional MLS visibility function in the comparison with the MLS observations, following *Jiang et al. [2004a]*.

[36] The comparison of the GWTVs from the ray-based parameterization and the MLS measurements can be summarized as follows:

[37] 1. The unfiltered GWTVs in the ray-based parameterizations are much larger than the MLS GWTVs, peaking in the equatorial regions where strong convection occurs.

[38] 2. The magnitude of the GWTVs is significantly reduced, especially in the equatorial regions, by applying the MLS visibility function. The magnitude and distribution of the MLS-filtered GWTVs in the ray-based parameterization are comparable to those of the MLS GWTVs.

[39] Even though the ray-based parameterization can reasonably reproduce the MLS GWTVs, it should be noted that several uncertainties still remain. The results of the ray-based parameterization are sensitive to the source-level wave propagation direction. The ray-based parameterization

can reasonably reproduce the MLS GWTVs when considering northeast-southwest or northwest-southeast propagation directions. On the other hand, the GWTVs are overestimated in the equatorial regions and underestimated in the summer subtropics when east-westward and north-southward propagating GWs alone are assumed. This indicates that the wave propagation direction is an important factor for obtaining realistic distributions and magnitudes of GW variances from the parameterization. Consequently, one must reasonably choose a wave propagation direction in order to achieve a realistic reproduction of the GW effects. Although we can assume that northeast-southwest or northwest-southeast is the true wave propagation direction (which is dominant in the summer subtropics, from the above results) because of their best reproduction against MLS GW measurements, realistic wave propagation directions and other relevant factors are still not well known.

[40] Recently, *Kuester et al. [2008]* simulated hurricanes and analyzed the dominant propagation direction of the convectively induced stratospheric GWs. They suggested that the dominant wave propagation direction is found via a difference between the source velocity vector and the wind vector at the cloud top. Similarly, S.-Y. Kim et al. (A study on stratospheric gravity waves generated by Typhoon Ewiniar: Numerical simulations and observations, submitted to *Journal of Geophysical Research*, 2009) analyzed the propagation directions of stratospheric GWs generated by typhoons. They showed, however, that wave propagation directions correspond to the source moving directions that satisfy the wave propagation conditions in the spectral regions. To determine the source-level wave propagation direction in the ray-based parameterization, we tested the following for wave propagation direction: (1) cloud moving direction according to S.-Y. Kim et al. (submitted manuscript, 2009), (2) background wind direction at the cloud top, and (3) the direction demonstrated by *Kuester et al. [2008]*. Comparison with the MLS, however, showed that none of the above modified methods can realistically reproduce the MLS GWTV. There are still uncertainties about factors that determine the wave propagation direction of convective GWs, eventually requiring further systematic studies.

[41] Another limitation of this study is that the comparison between the ray-based parameterization and MLS measurement is meaningful only within the long vertical and short horizontal wavelength portions of the GW spectra, where the GWs are largely visible to the MLS. Consequently, the realism of the ray-based parameterization cannot be fully tested by comparison with MLS measurements alone. Therefore, it is necessary to compare the ray-based parameterization with other observations that can cover different spectral ranges to obtain more general results. For example, GPS occultation can provide useful information for convective GWs in the spectral ranges not covered by MLS with its high global coverage [*Tsuda et al., 2000*]. The use of the other observations is also important to check the differences between the ray-based and columnar parameterizations. In this study, we found that the differences between the two parameterizations can be underestimated because of the weak MLS visibility for tropical GWs in the upper stratosphere, though unfiltered GWTV differences between the two parameterizations are not negligible in this region. Hence,

additional comparisons with other GW observations that are sensitive to equatorial GWs are required to clearly understand the difference between the two parameterizations.

[42] Finally, one should also perform validations over various heights, including the lower stratosphere, where convectively induced equatorial GWs are significant, and for different years and seasons as well. Further studies of these topics will be carried out in future works.

[43] **Acknowledgments.** This work was supported by the Ministry of Science and Technology of Korea through the National Research Laboratory Program (M10500000114-06J0000-11410). The DCH data set was provided by the cooperative research project of the NCEP-DOE Atmospheric Model Intercomparison Project (AMIP-II) reanalysis (R-2) by NCEP and DOE. The ECMWF ERA-40 reanalysis data set was provided by ECMWF from their data server.

## References

- Alexander, M. J. (1998), Interpretations of observed climatological patterns in stratospheric gravity wave variance, *J. Geophys. Res.*, **103**, 8627–8640, doi:10.1029/97JD03325.
- Alexander, M. J., and T. J. Dunkerton (1999), A spectral parameterization of mean-flow forcing due to breaking gravity waves, *J. Atmos. Sci.*, **56**, 4167–4182, doi:10.1175/1520-0469(1999)056<4167:ASPOMF>2.0.CO;2.
- Alexander, M. J., and H. Teitelbaum (2007), Observation and analysis of a large amplitude mountain wave event over the Antarctic peninsula, *J. Geophys. Res.*, **112**, D21103, doi:10.1029/2006JD008368.
- Alexander, M. J., et al. (2008), Global estimates of gravity wave momentum flux from High Resolution Dynamics Limb Sounder observations, *J. Geophys. Res.*, **113**, D15S18, doi:10.1029/2007JD008807.
- Beres, J. H. (2004), Gravity wave generation by a three-dimensional thermal forcing, *J. Atmos. Sci.*, **61**, 1805–1815, doi:10.1175/1520-0469(2004)061<1805:GWGBAT>2.0.CO;2.
- Beres, J. H., R. R. Garcia, B. A. Boville, and F. Sassi (2005), Implementation of a gravity wave source spectrum parameterization dependent on the properties of convection in the Whole Atmosphere Community Climate Model (WACCM), *J. Geophys. Res.*, **110**, D10108, doi:10.1029/2004JD005504.
- Chun, H.-Y., and J.-J. Baik (1998), Momentum flux by thermally induced internal gravity waves and its approximation for large-scale models, *J. Atmos. Sci.*, **55**, 3299–3310, doi:10.1175/1520-0469(1998)055<3299:MFBTII>2.0.CO;2.
- Chun, H.-Y., and J.-J. Baik (2002), An updated parameterization of convectively forced gravity wave drag for use in large-scale models, *J. Atmos. Sci.*, **59**, 1006–1017, doi:10.1175/1520-0469(2002)059<1006:AUPOCF>2.0.CO;2.
- Chun, H.-Y., M.-D. Song, J.-W. Kim, and J.-J. Baik (2001), Effects of gravity wave drag induced by cumulus convection on the atmospheric general circulation, *J. Atmos. Sci.*, **58**, 302–319, doi:10.1175/1520-0469(2001)058<0302:EOGWDI>2.0.CO;2.
- Chun, H.-Y., I.-S. Song, J.-J. Baik, and Y.-J. Kim (2004), Impact of a convectively forced gravity wave drag parameterization in NCAR CCM3, *J. Clim.*, **17**, 3530–3547, doi:10.1175/1520-0442(2004)017<3530:IOACFG>2.0.CO;2.
- Chun, H.-Y., H.-J. Choi, and I.-S. Song (2008), Effect of nonlinearity on convectively forced internal gravity waves: Application to a gravity wave drag parameterization, *J. Atmos. Sci.*, **65**, 557–575, doi:10.1175/2007JAS2255.1.
- Ern, M., P. Preusse, and M. J. Alexander (2004), Absolute values of gravity wave momentum flux derived from satellite data, *J. Geophys. Res.*, **109**, D20103, doi:10.1029/2004JD004752.
- Fetzer, E. J., and J. C. Gille (1994), Gravity wave variance in LIMS temperatures. Part I: Variability and comparison with background winds, *J. Atmos. Sci.*, **51**, 2461–2483, doi:10.1175/1520-0469(1994)051<2461:GWVILT>2.0.CO;2.
- Hines, C. O. (1997), Doppler-spread parameterization of gravity-wave momentum deposition in the middle atmosphere. Part I: Basic formulation, *J. Atmos. Sol. Terr. Phys.*, **59**, 371–386, doi:10.1016/S1364-6826(96)00079-X.
- Jiang, J. H., S. D. Eckermann, D. L. Wu, and J. Ma (2004a), A search for mountain waves in MLS stratospheric limb radiances from the winter Northern Hemisphere: Data analysis and global mountain wave modeling, *J. Geophys. Res.*, **109**, D03107, doi:10.1029/2003JD003974.
- Jiang, J. H., B. Wang, K. Goya, K. Hocke, S. D. Eckermann, J. Ma, D. L. Wu, and W. G. Read (2004b), Geographical distribution and interseasonal variability of tropical deep convection: UARS MLS observations and analyses, *J. Geophys. Res.*, **109**, D03111, doi:10.1029/2003JD003756.
- Jiang, J. H., S. D. Eckermann, D. L. Wu, K. Hocke, B. Wang, J. Ma, and Y. Zhang (2005), Seasonal variation of gravity wave sources from satellite observation, *Adv. Space Res.*, **35**, 1925–1932, doi:10.1016/j.asr.2005.01.099.
- Kanamitsu, M., W. Ebisuzaki, J. Woollen, S.-K. Yang, J. J. Hnilo, M. Fiorino, and G. L. Potter (2002), NCEP-DEO AMIP-II Reanalysis (R-2), *Bull. Am. Meteorol. Soc.*, **83**, 1631–1643, doi:10.1175/BAMS-83-11-1631(2002)083<1631:NAR>2.3.CO;2.
- Kiehl, J. T., J. J. Hack, G. B. Bonan, B. A. Boville, B. P. Briegleb, D. L. Williamson, and P. J. Rasch (1996), Description of the NCAR Community Climate Model (CCM3), *Tech. Note NCAR/TN-4201STR*, 152 pp., Natl. Cent. for Atmos. Res., Boulder, Colo.
- Kim, Y.-J., S. D. Eckermann, and H.-Y. Chun (2003), An overview of the past, present and future of gravity-wave drag parameterization for numerical climate and weather prediction models, *Atmos. Ocean*, **41**(1), 65–98, doi:10.3137/ao.410105.
- Kuester, M. A., M. J. Alexander, and E. A. Ray (2008), A model study of gravity waves over Hurricane Humberto (2001), *J. Atmos. Sci.*, **65**, 3231–3246, doi:10.1175/2008JAS2372.1.
- Lighthill, J. (1978), *Waves in Fluids*, 539 pp., Cambridge Univ. Press, Cambridge, U. K.
- Marks, C. J., and S. D. Eckermann (1995), A three-dimensional nonhydrostatic ray-tracing model for gravity waves: Formulation and preliminary results for the middle atmosphere, *J. Atmos. Sci.*, **52**, 1959–1984, doi:10.1175/1520-0469(1995)052<1959:ATDNRT>2.0.CO;2.
- McLandress, C., M. J. Alexander, and D. L. Wu (2000), Microwave Limb Sounder observations of gravity waves in the stratosphere: A climatology and interpretation, *J. Geophys. Res.*, **105**(D9), 11,947–11,967, doi:10.1029/2000JD900097.
- Preusse, P., et al. (2006), Tropopause to mesopause gravity waves in August: Measurement and modeling, *J. Atmos. Sol. Terr. Phys.*, **68**, 1730–1751, doi:10.1016/j.jastp.2005.10.019.
- Sassi, F., R. R. Garcia, B. A. Boville, and H. Liu (2002), On temperature inversions and the mesospheric surf zone, *J. Geophys. Res.*, **107**(D19), 4380, doi:10.1029/2001JD001525.
- Song, I.-S., and H.-Y. Chun (2005), Momentum flux spectrum of convectively forced internal gravity waves and its application to gravity wave drag parameterization. Part I: Theory, *J. Atmos. Sci.*, **62**, 107–124, doi:10.1175/JAS-3363.1.
- Song, I.-S., and H.-Y. Chun (2008), A Lagrangian spectral parameterization of gravity wave drag induced by cumulus convection, *J. Atmos. Sci.*, **65**, 1204–1224, doi:10.1175/2007JAS2369.1.
- Song, I.-S., H.-Y. Chun, and T. P. Lane (2003), Generation mechanisms of convectively forced internal gravity waves and their propagation to the stratosphere, *J. Atmos. Sci.*, **60**, 1960–1980, doi:10.1175/1520-0469(2003)060<1960:GMOCFI>2.0.CO;2.
- Song, I.-S., H.-Y. Chun, R. R. Garcia, and B. A. Boville (2007), Momentum flux spectrum of convectively forced internal gravity waves and its application to gravity wave drag parameterization. Part II: Impacts in a GCM (WACCM), *J. Atmos. Sci.*, **64**, 2286–2308, doi:10.1175/JAS3954.1.
- Tsuda, T., M. Nishida, C. Rocken, and R. Ware (2000), A global morphology of gravity wave activity in the stratosphere revealed by the GPS occultation data (GPS/MET), *J. Geophys. Res.*, **105**(D6), 7257–7274, doi:10.1029/1999JD901005.
- Uppala, S. M., et al. (2005), The ERA-40 re-analysis, *Q. J. R. Meteorol. Soc.*, **131**, 2961–3012, doi:10.1256/qj.04.176.
- Warner, C. D., and M. E. McIntyre (2001), An ultrasimple spectral parameterization for nonorographic gravity waves, *J. Atmos. Sci.*, **58**, 1837–1857, doi:10.1175/1520-0469(2001)058<1837:AUSPFN>2.0.CO;2.
- Wu, D. L. (2004), Mesoscale gravity wave variances from AMSU-A radiances, *Geophys. Res. Lett.*, **31**, L12114, doi:10.1029/2004GL019562.
- Wu, D. L., and S. D. Eckermann (2008), Global gravity wave variances from Aura MLS: Characteristics and interpretation, *J. Atmos. Sci.*, **65**, 3695–3718, doi:10.1175/2008JAS2489.1.
- Wu, D. L., and J. W. Waters (1996), Gravity-wave-scale temperature fluctuations seen by the UARS MLS, *Geophys. Res. Lett.*, **23**, 3289–3292, doi:10.1029/96GL02924.

H.-J. Choi and H.-Y. Chun, Department of Atmospheric Sciences, Yonsei University, 262 Seongsanno, Seodaemun-gu, Seoul 120-749, South Korea. (chunhy@yonsei.ac.kr)

I.-S. Song, Global Modeling and Assimilation Office, NASA Goddard Space Flight Center, Code 610.1, Building 33, Room C112, Greenbelt, MD 20771, USA.